Analysis and Design of a High Step-up Current-Fed Multiresonant DC–DC Converter With Low Circulating Energy and Zero-Current Switching for All Active Switches

Bo Yuan, *Student Member, IEEE*, Xu Yang, *Member, IEEE*, Xiangjun Zeng, Jason Duan, *Member, IEEE*, Jerry Zhai, and Donghao Li

***Abstract*—A high-efficiency high step-up current-fed multiresonant converter (CFMRC) is proposed for interfacing the sustainable power sources, such as PV panels and fuel cells, which are characterized by low-voltage high-current output and have strict current ripple requirement. The proposed converter has the features of low input current ripple, low circulating energy, achieving zero-current switching (ZCS) for all active switches, and common ground driving. In order to further improve the efficiency and the power density of the CFMRC, coupled inductor and voltage doubler are applied to the two input inductors and the output rectifier, respectively. The operation principle of the CFMRC is introduced. Its dc voltage gain and the ZCS conditions of both the primary switches and the secondary rectifier are also derived based on the steady-state analysis. Finally, a design guideline is given. The theoretical analysis of the CFMRC was verified on a 150-W prototype. An average efficiency of 95.9% was achieved over the entire maximum power point tracking range (23–38 V), with a 350-V output at full load.**

***Index Terms*—Coupled inductor, current-fed multiresonant converter (CFMRC), step-up converter, voltage doubler, zero-current switching (ZCS).**

I. Introduction

FOSSIL fuel related environmental issues and the challenges to sustainable industrialization stimulate the development of distributed generation based on renewable energy [1]–[14]. Some of the renewable power sources, such as PV panels and fuel cells, are characterized by low-voltage high-current output and have strict current ripple requirement [1]–[16]. Consequently, a dc–dc converter with high step-up capability, galvanic isolation, low input current ripple, and high efficiency is required.

Current-fed converters attract more and more interests in such kind of applications, with their inherent properties of high boost capability and small input current ripple. Thus, the transformer's turns ratio can be reduced, and the bulk input filters can be shrunk as compared with the conventional voltage-fed converters. However, the current-fed pulse width modulated converters [17]–[23] still have the problems of high voltage and current spikes resulting from the leakage inductance and winding capacitance of the transformer, and high voltage stress on the rectifying diodes due to their reverse recovery. Hence, their operating frequency should be low, and the power conversion efficiency is also limited. Kinds of active clamping techniques [15], [24]–[27] have been proposed to recycle the energy stored in the leakage inductance and to alleviate the surge voltage on the switches. Nevertheless, the additional clamping circuits complicate the application, lower the reliability, increase the cost, and always result in triangular switch currents which increase the current rms values.

Resonant techniques promise high-efficiency power conversion while operating at high switching frequency with their instinctive capability of well utilizing the circuit parasitics and achieving zero-voltage switching (ZVS) or zero-current switching (ZCS) for the active switches [28]–[32]. Moreover, the current-fed parallel resonant converters (CFPRCs) [33] also have high step-up feature, with the introduced LC parallel resonating driven by a square wave current source. With such techniques, not only the parasitics of the transformer can be utilized, but also the turns ratio can be further reduced. Most of the efforts for the CFPRCs were focused on achieving ZVS of the primary switches no matter if the active switches were controlled with dead time [34]–[36] or overlapping [37]–[39]. However, in low-voltage high-current input applications, ZVS is not that much important, while ZCS is the key for switching loss elimination [40]–[42], whereas the existing leakage inductance of the transformer still causes high voltage spikes on the switches. References [41] and [42] proposed a resonance between the leakage inductance and the parallel resonant capacitor to achieve ZCS turn-off and to reduce the voltage stress

Manuscript received August 6, 2010; revised December 31, 2010 and March 11, 2011; accepted April 26, 2011. Date of publication May 31, 2011; date of current version October 18, 2011.

B. Yuan was with the State Key Laboratory of Electrical Insulation and Power Equipment, Xi'an Jiaotong University, Xi'an, Shaanxi 710049, China. He is now with the Power Management Products Division, Analog Devices, Inc., Xi'an, Shaanxi 710075, China (e-mail: Bob.Yuan@analog.com).

X. Yang and D. Li are with the State Key Laboratory of Electrical Insulation and Power Equipment, Xi'an Jiaotong University, Xi'an, Shaanxi 710049, China (e-mail: yangxu@mail.xjtu.edu.cn; lidonghao1986@163.com).

X. Zeng (corresponding author) is with the School of Electrical Engineering, Xi'an Jiaotong University, Xi'an, Shaanxi 710049, China (e-mail: zengxj@mail.xjtu.edu.cn).

J. Duan and J. Zhai are with the Department of Power Management Products, Analog Devices, Inc., Shanghai 200021, China (e-mail: Jason.Duan@analog.com; jerry.zhai@analog.com).

Color versions of one or more of the figures in this paper are available online at http://ieeexplore.ieee.org.

Digital Object Identifier 10.1109/TIE.2011.2158036

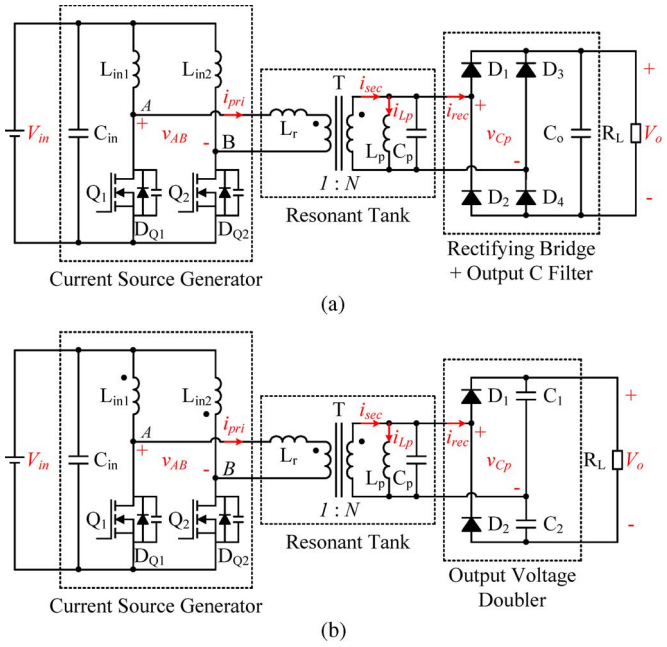

Fig. 1. Schematics of the proposed converter. (a) Without coupled inductor and with full-bridge rectifier. (b) With coupled inductor and with voltage doubler.

for all primary switches. Nevertheless, in order to achieve full load range ZCS of the primary switches, the leakage inductance was manipulated according to the heavy load condition, which would result in a large redundant circulating current flowing through the antiparallel diodes of the switches and, hence, the greatly reduced efficiency at light load. Large circulating energy within the resonant tank also produces high conduction losses and limits the efficiency improvement of the CFPRCs. Energy feedback was proposed to reduce the circulating energy [43]. However, the necessary extra transformer and its impact on the quality factor make this concept inapposite for a design with high density and voltage regulation requirements. Moreover, the reverse recovery issue of the rectifying diodes still exists and results in high voltage spikes on the rectifying diodes. This limits the application of ultrafast recovery diodes with lower voltage rating and lower forward voltage drop.

In this paper, a high-efficiency high step-up current-fed multiresonant dc–dc converter with low input current ripple is proposed, as shown in Fig. 1. The proposed converter consists of a square wave current source generator, a multiresonant tank, and an output voltage doubler [15], [26]. The current-fed half-bridge structure is adopted as the square wave current source generator, with its inherent merits of low input current ripple, low primary current of the transformer, high step-up capability, and common ground gate driving. With the expectation of further improving the efficiency and reducing the size of the converter, coupled inductor techniques [19], [44] were finally applied to the two input inductors. The multiresonant tank offers high voltage gain to reduce the turns ratio of the transformer. Meanwhile, it absorbs both the self-winding capacitances of the transformer and the junction capacitances of the rectifying diodes into its resonant capacitor; thus, the current spikes within the circuit are well suppressed. By operating the two primary switches with overlapped conduction time, a resonance between the leakage inductance and the resonant capacitor is introduced during the overlapping interval to achieve soft commutation of the primary current which finally flows through the antiparallel diode before the switch turning off. Thereby, the primary switches are turned off with ZCS, and the voltage spikes across the switches are reduced. The adopted single-capacitor output filter clamps the peak voltage of the resonant capacitor to the output voltage during the conduction period of the rectifying diodes, whereas during the nonconduction period, the voltage of the resonant capacitor could resonate down. In this way, the circulating energy within the resonant tank and the related conduction losses are reduced, the overshooting of the primary current is limited, and ZCS is achieved for the rectifying diodes without any additional efforts in full load range. For efficiency improvement, a voltage doubler was finally selected instead of the full-bridge rectifier.

The detailed operation principle of the proposed converter is introduced in Section II. Section III carries out a comprehensive steady-state analysis. The dc voltage gain and the ZCS conditions for all active switches are derived. Section IV develops a design guideline for the proposed converter. Section V demonstrates the theoretical analysis of the proposed converter on a 150-W prototype. Finally, Section VI concludes this paper.

II. Operation Principle Description

As shown in Fig. 1(b), the current-fed half-bridge structure includes two input inductors $L_{\rm in1}$ and $L_{\rm in2}$ and two active switches $\rm Q_1$ and $\rm Q_2$. $\rm D_{Q1}$ and $\rm D_{Q2}$ are the antiparallel diodes of $\rm Q_1$ and $\rm Q_2$, respectively. The multiresonant tank consists of a resonant capacitor C_p, a first resonant inductor L_p, and a second resonant inductor L_r which participates in the resonance together with L_p and C_p only during the commutation period of the primary current $i_{\rm pri}$. L_p is performed by the transformer's magnetizing inductance which is much larger than L_r. The transformer's leakage inductance and self-winding capacitance are incorporated into L_r and C_p, respectively. The junction capacitances of the secondary rectifying diodes $\rm D_1$ and $\rm D_2$ are also absorbed into C_p. The output capacitors C_1 and C_2 are much larger than C_p and can smooth the rectified resonant capacitor voltage v_{Cp}.

In order to clarify the illustration and analysis of the proposed converter, several assumptions are first made. $L_{\rm in1}$, $L_{\rm in2}$, C_1, and C_2 are sufficiently large so that the input current $I_{\rm in}$ and the output voltage V_o are constant during one switching cycle. The active switches $\rm Q_1$ and $\rm Q_2$ and the diodes, including $\rm D_{Q1}$ and $\rm D_{Q2}$, are ideal. The parasitics of all passive components are not considered here.

Fig. 2(a)–(f) shows the first six operation modes of the proposed converter during half switching cycle, and the other six operation modes for the remaining half switching cycle are symmetrical to the first six operation modes. Fig. 2(g) shows the corresponding theoretical waveforms.

Before t_0, $\rm Q_1$ is on, $\rm Q_2$ is off, $L_{\rm in1}$ is charged by the input voltage $V_{\rm in}$, and $L_{\rm in2}$ transfers its stored energy to the load through $\rm D_2$. v_{Cp} is clamped to $-V_o/2$, and L_p is linearly discharged. The current flowing through $\rm D_2$ (i_{D2}) is equal to the transformer's secondary current $i_{\rm sec}$ minus the current flowing through L_p (i_{Lp}).

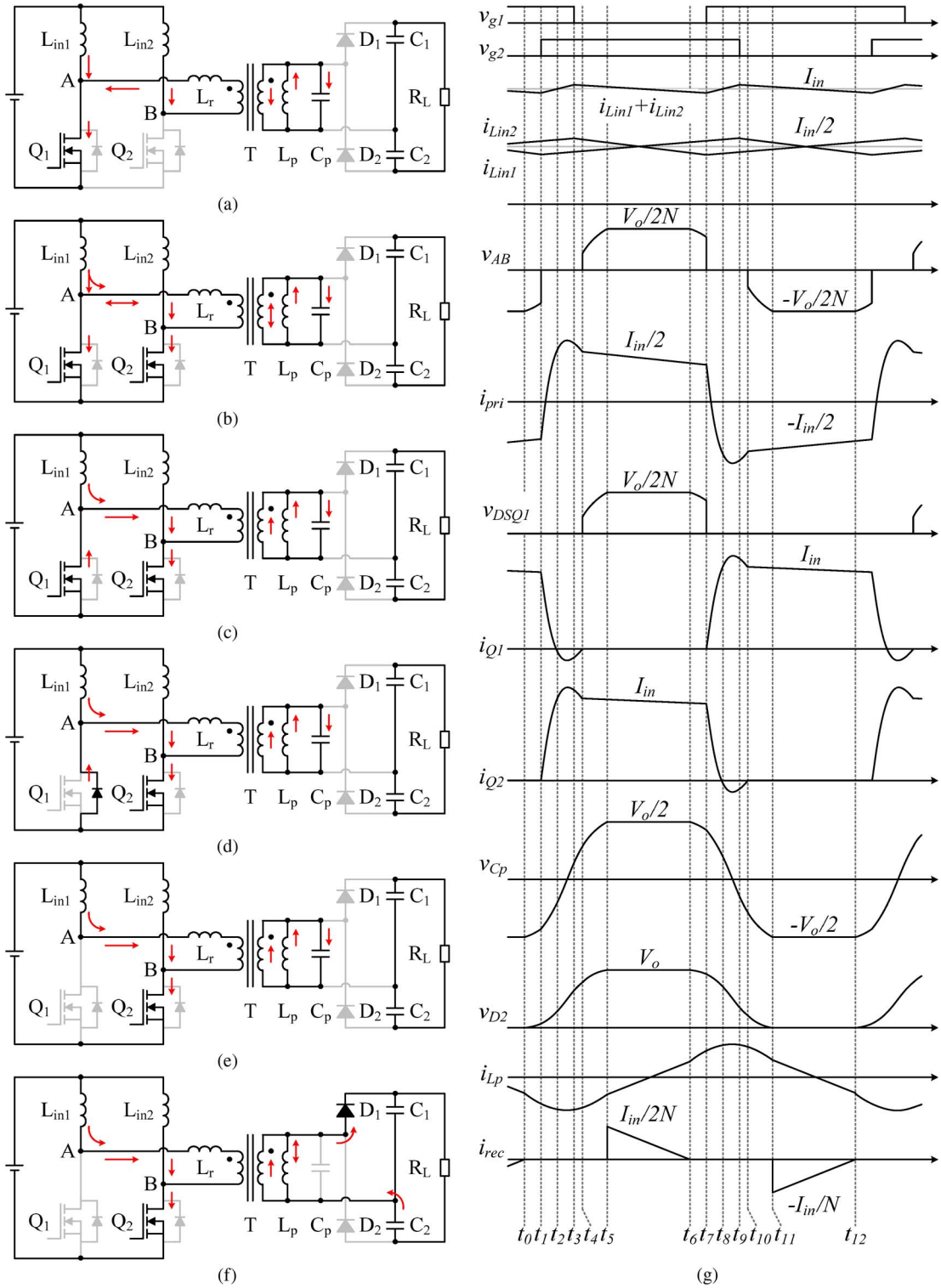

Fig. 2. Operating modes and waveforms of the proposed converter. (a) Mode 1. (b) Mode 2. (c) Mode 3. (d) Mode 4. (e) Mode 5. (f) Mode 6. (g) Theoretical waveforms.

Mode 1 [t_0–t_1; Fig. 2(a)]: At t_0, i_{Lp} is equal to $i_{\rm sec}$, and i_{D2} drops to zero. From t_0 on, Q_1 keeps on, Q_2 keeps off, all rectifying diodes are off, the current flowing through $L_{\rm in2}$ (i_{Lin2}) feeds the resonant tank formed by L_p and C_p, and L_r is absorbed into $L_{\rm in2}$. Mode 1 ends at t_1 when Q_2 is switched on. In mode 1, $L_{\rm in1}$ is charged by $V_{\rm in}$, and v_{Cp} resonates up.

Mode 2 [t_1–t_2; Fig. 2(b)]: From t_1 on, both Q_1 and Q_2 conduct the current, terminals A and B are shorted, and all of the rectifying diodes keep on blocking. L_r participates the resonance of L_p and C_p for the commutation of $i_{\rm pri}$. As $i_{\rm pri}$ oscillating from negative to positive is driven by the initial negative v_{Cp} at t_1, current flowing through Q_2 (i_{Q2}) increases, while current flowing through Q_1 (i_{Q1}) decreases.

When i_{Q1} reaches zero at t_2, mode 2 ends. It is critical to select a proper L_r based on the overlap time to ensure that i_{Q1} would drop to zero but with little overshooting, and then, Q_1 could be turned off in the ZCS condition with minimized circulating energy. During this period, L_{in1} and L_{in2} are both charged by V_{in}, and v_{Cp} keeps on resonating up.

Mode 3 [t_2–t_3; Fig. 2(c)]: This mode is similar to mode 2, while i_{Q1} goes negative. Mode 3 ends at t_3 when Q_1 gets off. In this interval, i_{pri} and i_{Lp} come to their peaks, respectively, and v_{Cp} rises across zero but is lower than $V_o/2$.

Mode 4 [t_3–t_4; Fig. 2(d)]: This mode is similar to mode 3 except that the negative i_{Q1} flows through D_{Q1} after Q_1 is off. When i_{Q1} reaches zero again at t_4, mode 4 ends. This period is expected to be minimized by properly controlling the turn-off point of Q_1 to eliminate the conduction loss on D_{Q1}.

Mode 5 [t_4–t_5; Fig. 2(e)]: From t_4 on, D_{Q1} blocks off, while Q_2 keeps on. L_r is absorbed into L_{in1}, and the current flowing through L_{in1} (i_{Lin1}) feeds the resonant tank formed by L_p and C_p, while L_{in2} is still charged by V_{in}. Mode 5 ends at t_5 when v_{Cp} touches $V_o/2$.

Mode 6 [t_5–t_6; Fig. 2(f)]: From t_5 on, Q_1 is off, Q_2 is on, D_1 is forced on, and v_{Cp} is clamped to $V_o/2$. L_{in1} transfers its stored energy to the load, while L_{in2} is charged by V_{in}. L_p is charged by $V_o/2$. The current flowing through D_1 (i_{D1}) is equal to i_{sec} minus i_{Lp}. Mode 6 ends at t_6 when i_{Lp} is equal to i_{sec} and i_{D1} drops to zero. Because v_{Cp} is clamped to $V_o/2$ during this energy transferring period which takes up most part of the half switching cycle, the circulating energy within L_p and C_p is minimized, and the related conduction losses are accordingly reduced. As i_{sec} is almost constant during this period, the decreasing slew rate of i_{D1} is dominated by the well-controlled i_{Lp}; hence, ZCS can be ideally achieved for D_1, and the reverse recovery issue is well eliminated without any additional efforts. The same situation is also applied to D_2. Subsequently, the general ultrafast silicon diodes with low forward voltage drop could be adopted by the rectifying diodes for better conduction performance, lower cost, and higher reliability.

III. Steady-State Analysis

As illustrated in Section II, there are two kinds of resonances in the proposed current-fed multiresonant converter (CFMRC). L_r and C_p dominate the first kind of resonance during the commutation of i_{pri} from t_1 to t_4 (modes 2–4). During this period, L_p is parallel with L_r and participates the resonance with C_p. However, L_p is performed by the transformer's magnetizing inductance, while L_r would just be the leakage inductance. L_p is much (more than 40 times in the experiment in Section V) larger than L_r; thereby, L_p has little affection and can be ignored in this first kind of resonance. For the second kind of resonances during t_0–t_1 (modes 1) and t_4–t_5 (modes 5), L_r is absorbed into L_{in1}, or L_{in2} and has no effect, while L_p resonates with C_p to offer a high impedance to the current source to generate the required high voltage.

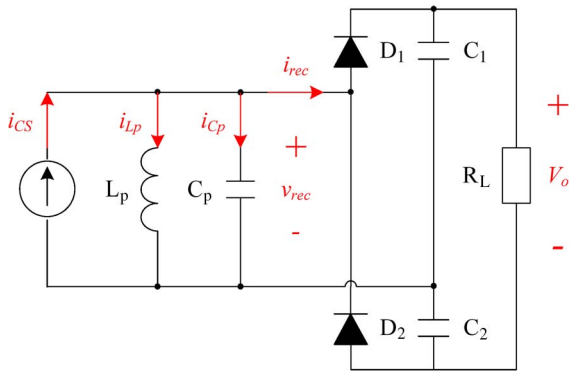

Fig. 3. Simplified circuit model of the proposed converter.

Obviously, L_r only affects the commutation of i_{pri}. Fast and soft commutation of i_{pri} is ensured by the proper design of L_r. In this condition, the input voltage source and the current-fed half-bridge together with L_r can be modeled as a symmetrical square wave current source (Fig. 3) to simplify the steady-state analysis. In Fig. 3, the square wave current source is transferred to the secondary side of the transformer and has a magnitude of $I_{in}/2N$, where N represents the turns ratio of the transformer. Such simplification would be accurate enough especially for the derivation of the dc voltage gain characteristics of the proposed converter as no power is transferred to the load during the commutation period of i_{pri}. However, L_r and the commutation of i_{pri} are critical in achieving ZCS for the two primary switches, which will be deeply investigated later.

A. Analytical Solution of the Simplified Circuit Model

For the simplified circuit model shown in Fig. 3, four operation states are identified, and the key waveforms are shown in Fig. 4.

In the first state, both of the rectifying diodes block the load current, and the square wave current source i_{CS} feeds the resonant tank formed by C_p and L_p. The waveform of i_{Lp} presents part of sinusoidal, and it could be expressed as

$$i_{Lp}(t) = I_{Lp\_pk} \sin(\omega_p t - \varphi), \qquad \frac{\pi}{2} < \varphi < \pi \tag{1}$$

where I_{Lp_pk} is the peak value of i_{Lp}, φ represent its phase angle, and

$$\omega_p = \frac{1}{\sqrt{L_p C_p}}. \tag{2}$$

In the second state, D_1 conducts the load current, i_{CS} feeds the load, the resonant tank voltage v_{rec} is clamped to $V_o/2$, and L_p is linearly charged by $V_o/2$. For the purpose of making the following analysis brief and clear, a conducting angle θ is defined to represent this conducting interval, and then, the aforementioned resonant interval could be represented by $\pi - \theta$. The remaining two states are symmetrical to the previous two states. In order to simplify the derivation of the analytical solution for the simplified circuit model shown in Fig. 3, the following formula deduction begins from the conducting interval.

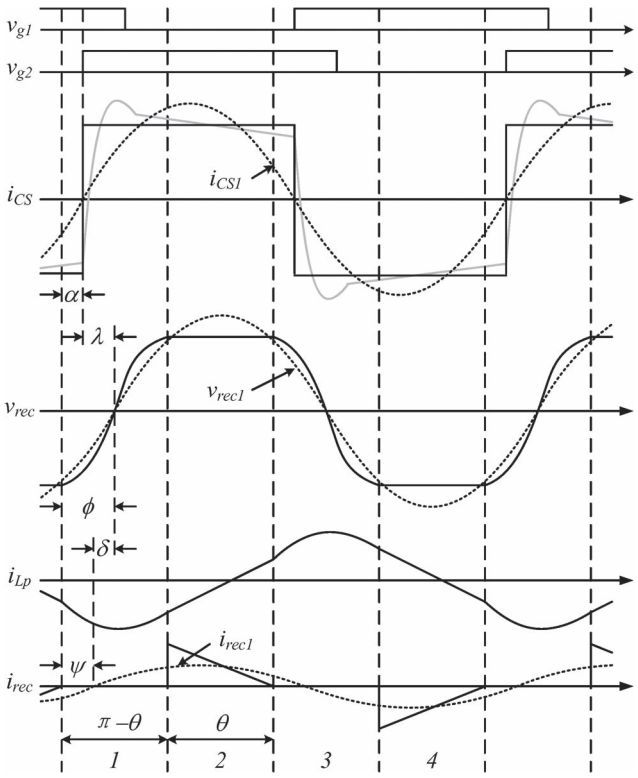

Fig. 4. Key waveforms of the simplified circuit model.

During the conducting interval $[\pi-\theta$ to $\pi]$

$$i_{\rm rec}(t) = i_{CS}(t) - i_{Lp}(t) \tag{3}$$

$$i_{CS}(t) = \frac{I_{\rm in}}{2N} \tag{4}$$

$$i_{Lp}(t) = I_{Lp\_\rm bot} + \frac{v_{\rm rec}(t)}{L_p}\left(t - \frac{\pi-\theta}{\omega}\right) \tag{5}$$

$$v_{\rm rec}(t) = V_o/2 \tag{6}$$

where $i_{\rm rec}$ is the output current of the resonant tank, $I_{Lp\_\rm bot}$ is the bottom value of i_{Lp} during the conducting interval, and ω represents the angular switching frequency.

This conducting interval ends at the time of π/ω when i_{Lp} is equal to i_{CS} and $i_{\rm rec}$ drops to zero

$$i_{\rm rec}\left(\frac{\pi}{\omega}\right) = 0. \tag{7}$$

From (3)–(7), $I_{Lp\_\rm bot}$ and $i_{\rm rec}$ are obtained as

$$I_{Lp\_\rm bot} = \frac{I_{\rm in}}{2N} - \frac{\theta V_o}{2\omega L_p} \tag{8}$$

$$i_{\rm rec}(t) = -\frac{V_o}{2L_p}\left(t - \frac{\pi}{\omega}\right). \tag{9}$$

The load current I_o is equal to the average current flowing through the rectifier $(I_{\rm rec\_}av)$

$$I_o = I_{\rm rec\_}av = \frac{1}{\frac{\pi}{\omega}} \int_{\frac{\pi-\theta}{\omega}}^{\frac{\pi}{\omega}} i_{\rm rec}(t)\,dt. \tag{10}$$

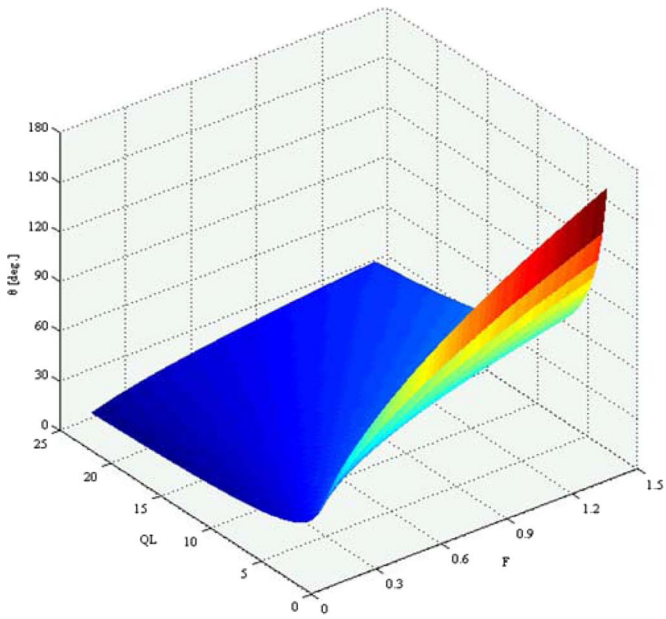

Fig. 5. Conducting angle θ as a function of F and Q_L.

By substituting (9) into (10)

$$I_o = I_{\rm rec\_}av = \frac{V_o\theta^2}{4\pi\omega L_p}. \tag{11}$$

On the other hand

$$I_o = \frac{V_o}{R_L} \tag{12}$$

where R_L represents the load resistance.

From (11) and (12), θ is obtained as

$$\theta = 2\sqrt{\frac{\pi F}{Q_L}} \tag{13}$$

where

$$F = \frac{\omega}{\omega_p} \tag{14}$$

$$Q_L = \frac{R_L}{Z_p} \tag{15}$$

$$Z_p = \sqrt{\frac{L_p}{C_p}}. \tag{16}$$

Formula (13) could be further shown by Fig. 5. It is clear that θ increases with the increasing of the load, and it can be well controlled by modulating the switching frequency.

During the resonant interval [0 to $\pi-\theta$]

$$i_{\rm rec}(t) = 0. \tag{17}$$

i_{Lp} is expressed as equation (1), and the current flowing through C_p is

$$i_{Cp}(t) = i_{CS}(t) - i_{Lp}(t). \tag{18}$$

The resonant tank voltage $v_{\rm rec}$ is

$$v_{\rm rec}(t) = v_{Cp}(t) = \frac{1}{C_p}\int i_{Cp}(t)\,dt. \tag{19}$$

The boundary conditions of the resonant interval are

$$i_{Lp}(0) = -\frac{I_{\rm in}}{2N} \tag{20}$$

$$v_{\rm rec}(0) = v_{Cp}(0) = -V_o/2 \tag{21}$$

$$i_{Lp}\left(\frac{\pi-\theta}{\omega}\right) = I_{Lp\_\rm bot} \tag{22}$$

$$v_{\rm rec}\left(\frac{\pi-\theta}{\omega}\right) = v_{Cp}\left(\frac{\pi-\theta}{\omega}\right) = V_o/2. \tag{23}$$

From (1), (8), (20), and (22), φ and I_{Lp_pk} are obtained as

$$\varphi = \pi + \tan^{-1}\left(\frac{\sin\left(\frac{\pi-\theta}{F}\right)}{1-\frac{NV_o\theta}{Z_pI_{\rm in}F}+\cos\left(\frac{\pi-\theta}{F}\right)}\right) \tag{24}$$

$$I_{Lp\_pk} = \frac{I_{\rm in}}{2N}\sqrt{1+\frac{\left[1-\frac{NV_o\theta}{Z_pI_{\rm in}F}+\cos\left(\frac{\pi-\theta}{F}\right)\right]^2}{\sin^2\left(\frac{\pi-\theta}{F}\right)}}. \tag{25}$$

Because i_{CS} changes its polarity during the resonant interval, it is necessary to deduce $v_{\rm rec}$ by dividing a whole resonant interval into two periods for more detailed investigation. The first period is defined from the beginning of the resonant interval to the point when i_{CS} changes its polarity, and α is used to represent this period with an angular unit of measure.

In this first resonant period [0 to α]

$$i_{CS}(t) = -\frac{I_{\rm in}}{2N}. \tag{26}$$

From (1), (18), (19), (21), and (26), $v_{\rm rec}$ is obtained as

$$v_{\rm rec}(t) = -\frac{Z_pI_{\rm in}}{2N}\omega_pt + Z_pI_{Lp\_pk}[\cos(\omega_pt-\varphi)-\cos(\varphi)]-V_o/2. \tag{27}$$

Accordingly, the remaining resonant interval is defined as the second resonant period [α to $\pi-\theta$]

$$i_{CS}(t) = \frac{I_{\rm in}}{2N}. \tag{28}$$

The initial condition of this period could be obtained from the final condition of the first resonant period

$$v_{\rm rec}\left(\frac{\alpha}{\omega}\right) = -\frac{Z_pI_{\rm in}\alpha}{2NF} + Z_pI_{Lp\_pk}\left[\cos\left(\frac{\alpha}{F}-\varphi\right)-\cos(\varphi)\right]-V_o/2. \tag{29}$$

From (1), (18), (19), (28), and (29), $v_{\rm rec}$ is obtained as

$$v_{\rm rec}(t) = \frac{Z_pI_{\rm in}}{2N}\left(\omega_pt-\frac{2\alpha}{F}\right) + Z_pI_{Lp\_pk}\left[\cos\left(\omega_pt-\varphi\right)-\cos(\varphi)\right]-V_o/2. \tag{30}$$

From (23)–(25) and (30), α is obtained as

$$\alpha = \frac{\pi-\theta}{2} - \frac{NV_oF}{Z_pI_{\rm in}}\left[1-\frac{\theta}{2F}\tan\left(\frac{\pi-\theta}{2F}\right)\right]. \tag{31}$$

B. DC Voltage Gain of the Proposed Converter

It is especially important to reveal the gain characteristics of a resonant converter for an adaptive control. The basis in deriving the gain characteristics is the power balance concept and the acknowledgement that the first harmonics of the voltage and current of the resonant tank are the main contributions to power transferring [45]–[48].

The first harmonics of i_{CS} (i_{CS1}, shown as the dashed line in Fig. 4) is

$$i_{CS1} = I_{CS1\_pk}\sin(\omega t-\alpha) \tag{32}$$

where

$$I_{CS1\_pk} = \frac{2I_{\rm in}}{\pi N}. \tag{33}$$

In order to find out the first harmonics of $v_{\rm rec}$ and $i_{\rm rec}$ ($v_{\rm rec1}$ and $i_{\rm rec1}$, shown as the dashed lines in Fig. 4), $v_{\rm rec}$ and $i_{\rm rec}$ are rewritten as (34), shown at the bottom of this page, and

$$i_{\rm rec}(t) = \begin{cases} 0, & 0 \le t < \frac{\pi-\theta}{\omega} \\ -\frac{\omega_pV_o}{2Z_p}\left(t-\frac{\pi}{\omega}\right), & \frac{\pi-\theta}{\omega} \le t \le \frac{\pi}{\omega}. \end{cases} \tag{35}$$

Then, $v_{\rm rec1}$ and $i_{\rm rec1}$ are obtained as

$$v_{\rm rec1}(t) = V_{\rm rec1\_pk}\sin(\omega t+\phi) \tag{36}$$

$$i_{\rm rec1}(t) = I_{\rm rec1\_pk}\sin(\omega t+\psi) \tag{37}$$

where $V_{\rm rec1\_pk}$, ϕ, $I_{\rm rec1\_pk}$, and Ψ can be easily derived by the Fourier series expansion.

Then, the phase shift between $v_{\rm rec1}$ and $i_{\rm rec1}$ can be obtained as

$$\delta = \phi - \psi. \tag{38}$$

The relationship between δ and F in different load conditions is shown in Fig. 6.

As δ is negative in the possible operation region, i.e., $i_{\rm rec1}$ leads $v_{\rm rec1}$, the resonant tank's equivalent load impedance could be modeled as an equivalent capacitor C_e together with a paralleled equivalent resistor R_e [45], [46]. Accordingly, an equivalent ac circuit of the simplified circuit model is obtained, as shown in Fig. 7.

$$v_{rec}(t) = \begin{cases} -\frac{Z_pI_{in}}{2N}\omega_pt + Z_pI_{Lp\_pk}\left[\cos\left(\omega_pt-\varphi\right)-\cos\left(\varphi\right)\right]-V_o/2, & 0 \le t < \frac{\alpha}{\omega} \\ \frac{Z_pI_{in}}{2N}\left(\omega_pt-\frac{2\alpha}{F}\right)+Z_pI_{Lp\_pk}\left[\cos\left(\omega_pt-\varphi\right)-\cos\left(\varphi\right)\right]-V_o/2, & \frac{\alpha}{\omega} \le t < \frac{\pi-\theta}{\omega} \\ V_o/2, & \frac{\pi-\theta}{\omega} \le t \le \frac{\pi}{\omega} \end{cases} \tag{34}$$

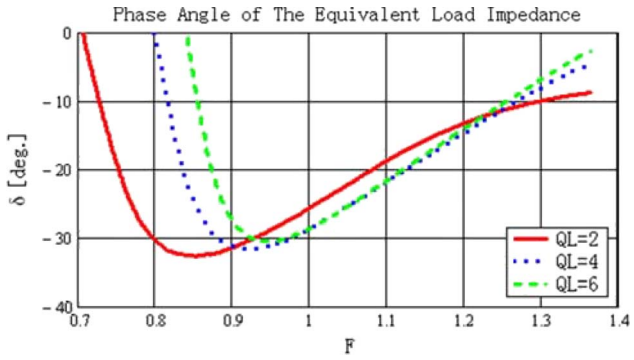

Fig. 6. Phase angle δ of the equivalent load impedance.

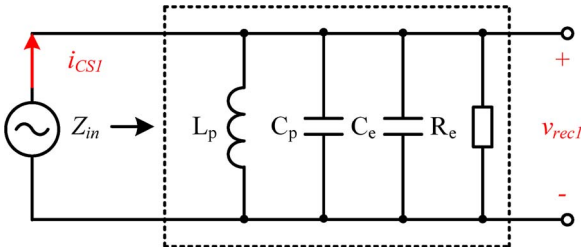

Fig. 7. Equivalent ac circuit of the simplified circuit model.

The power dissipation on R_e must be equal to the output power of the converter

$$\frac{V_o^2}{R_L} = \frac{V_{\mathrm{rec1\_}pk}^2}{2R_e} \tag{39}$$

where $v_{\mathrm{rec1\_}pk}$ is the peak value of v_{rec1}.

R_e is then obtained as

$$R_e = \frac{V_{\mathrm{rec1\_}pk}^2}{2V_o^2} R_L. \tag{40}$$

Moreover, with the relationship

$$\tan(|\delta|) = \omega C_e R_e. \tag{41}$$

C_e is obtained as

$$C_e = \frac{2V_o^2 \tan(|\delta|)}{\omega R_L V_{\mathrm{rec1\_}pk}^2}. \tag{42}$$

In Fig. 7, Z_{in} represents the input impedance of the equivalent ac circuit. Its amplitude is

$$|Z_{\mathrm{in}}| = \frac{V_{\mathrm{rec1\_}pk}}{I_{CS1\_pk}} = \frac{Q_e Z_p}{\sqrt{1+\left[Q_e\left(\frac{1}{F}-F\right)-\tan(|\delta|)\right]^2}} \tag{43}$$

where

$$Q_e = \frac{R_e}{Z_p}. \tag{44}$$

Supposing the efficiency of the proposed converter is η, then

$$P_o = \frac{V_o^2}{R_L} = \eta P_{\mathrm{in}} = \eta V_{\mathrm{in}} I_{\mathrm{in}}. \tag{45}$$

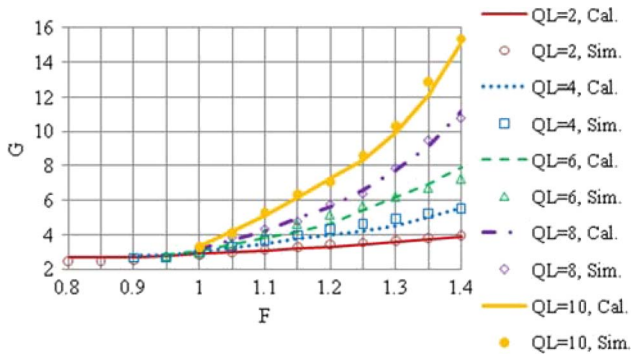

Fig. 8. DC voltage gain characteristics.

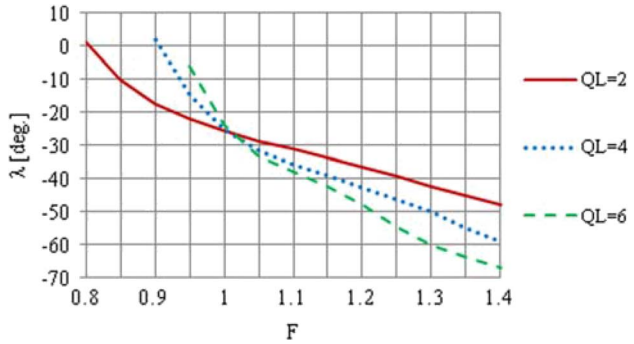

Fig. 9. Input phase angle λ.

From (33), (39), and (43)–(45), the dc voltage gain $G = V_o/V_{\mathrm{in}}$ of the proposed converter is obtained as

$$G = \pi\eta N\sqrt{\frac{2Q_L}{Q_e}}\sqrt{1+\left[Q_e\left(\frac{1}{F}-F\right)-\tan(|\delta|)\right]^2}. \tag{46}$$

Suppose $\eta = 1$ and $N = 1$, the dc voltage gain characteristics of the proposed converter are then revealed in Fig. 8. The calculated results based on (46) and the cycle-by-cycle simulated results are marked with lines and points, respectively. For each Q_L, the dc voltage gain curve stops at the bottom limitation of the operating frequency determined by the ZCS condition of the primary switches, as will be illustrated in the following part.

C. Input Phase Angle of the Equivalent AC Circuit

Another important property of a resonant converter is the input phase angle λ, i.e., the phase shift between the first harmonics of the tank voltage v_{AB} and the primary current i_{pri}. In the equivalent ac circuit of the simplified circuit model, the first harmonics of v_{AB} (v_{AB1}) is in phase with v_{rec1}, and the first harmonics of i_{pri} (i_{pri1}) is in phase with i_{cs1}. Hence, from Fig. 7

$$\lambda = \tan^{-1}\left(Q_e\left(\frac{1}{F}-F\right)-\tan(|\delta|)\right). \tag{47}$$

Formula (47) is also shown in Fig. 9.

D. ZCS Condition of Two Primary Switches

Achieving soft commutation of $i_{\rm pri}$ is essential for the ZCS operation of Q_1 and Q_2. The condition for the soft commutation of $i_{\rm pri}$ is that $i_{\rm pri}$ leads v_{AB}, i.e., λ should be negative, and that there is enough energy stored in C_p to help the commutation of $i_{\rm pri}$. During the commutation period of $i_{\rm pri}$, L_r resonates with C_p (here, L_p is neglected as it is always much larger than L_r). Thereby, the condition for the soft commutation of $i_{\rm pri}$ is obtained as

$$\lambda < 0 \tag{48}$$

$$\frac{1}{2}C_p v_{Cp}^2\left(\frac{\alpha}{\omega}\right) \geq L_r\left(\frac{I_{\rm in}}{2}\right)^2. \tag{49}$$

Criterion (48), together with Fig. 9, indicates the bottom limitation of the operating frequency. It is preferable to always run the switching frequency above the resonant frequency to ensure the soft commutation of $i_{\rm pri}$ in full load range, although a larger operating frequency range would be available with precise control.

Criterion (49) indicates the design criterion for L_r as

$$L_r \leq \frac{2C_p v_{Cp}^2\left(\frac{\alpha}{\omega}\right)}{I_{\rm in}^2}. \tag{50}$$

A maximum value of L_r ($L_{r\_\max}$) is then set by (50). If L_r is designed to be larger than $L_{r\_\max}$, the soft commutation of $i_{\rm pri}$ would be failed. On the other hand, if L_r is designed to be much smaller than $L_{r\_\max}$, the energy stored in C_p would cause too much overshooting of $i_{\rm pri}$, and the related circulating energy would induce extra conduction losses which reduce the power conversion efficiency.

With the soft commutation of $i_{\rm pri}$, the ZCS operation of Q_1 and Q_2 can be achieved by properly controlling their overlapped conduction time ΔT_{ov} as

$$\Delta T_{1,2} \leq \Delta T_{ov} \leq \Delta T_{1,4} \tag{51}$$

where

$$\Delta T_{1,2} = t_2 - t_1 \tag{52}$$

$$\Delta T_{1,4} = t_4 - t_1 \tag{53}$$

$$\Delta T_{ov} = (D - 0.5)\,T \tag{54}$$

and T represents the switching period. Subsequently, the limitation for the duty cycle D is obtained as

$$D_{\min} = \frac{\Delta T_{1,2}}{T} + 0.5 \tag{55}$$

$$D_{\max} = \frac{\Delta T_{1,4}}{T} + 0.5. \tag{56}$$

For the purpose of correctly controlling ΔT_{ov}, two criteria time periods $\Delta T_{1,2}$ and $\Delta T_{1,4}$ should be calculated. A simplified circuit model for the analysis of $i_{\rm pri}$ during the commutation period can be derived, as shown in Fig. 10.

Here, C_p' is the equivalent value of C_p referred to the primary side of the transformer

$$C_p' = N^2 C_p. \tag{57}$$

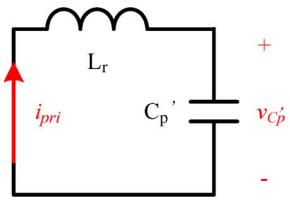

Fig. 10. Simplified circuit model for the analysis of $i_{\rm pri}$ during the commutation period.

At t_1, the initial conditions of this resonant circuit are

$$i_{\rm pri}(t_1) = -\frac{I_{\rm in}}{2} \tag{58}$$

$$v_{C'p}(t_1) = \frac{1}{N}v_{Cp}\left(\frac{\alpha}{\omega}\right). \tag{59}$$

From t_1 to t_4, L_r resonates with C_p', and the related differential equations are

$$-v_{C'p}(t) = L_r\frac{di_{\rm pri}(t)}{dt} \tag{60}$$

$$i_{\rm pri}(t) = C_p'\frac{dv_{C'p}(t)}{dt}. \tag{61}$$

Then, $i_{\rm pri}$ could be solved as

$$i_{\rm pri}(t) = -\frac{I_{\rm in}}{2}\cos\left(\omega_r(t-t_1)\right) - \frac{1}{NZ_r}v_{Cp}\left(\frac{\alpha}{\omega}\right)\sin\left(\omega_r(t-t_1)\right) \tag{62}$$

where

$$\omega_r = \frac{1}{\sqrt{L_r C_p'}} \tag{63}$$

$$Z_r = \sqrt{\frac{L_r}{C_p'}}. \tag{64}$$

At t_1 and t_4, here comes the following equation:

$$i_{\rm pri}(t) = \frac{I_{\rm in}}{2}. \tag{65}$$

Finally, $\Delta T_{1,2}$ and $\Delta T_{1,4}$ could be calculated as

$$\Delta T_{1,2} = \frac{1}{\omega_r}\sin^{-1}\left(\frac{-4NZ_r I_{\rm in} v_{Cp}\left(\frac{\alpha}{\omega}\right)}{N^2 Z_r^2 I_{\rm in}^2 + 4v_{Cp}^2\left(\frac{\alpha}{\omega}\right)}\right) \tag{66}$$

$$\Delta T_{1,4} = \frac{\pi}{\omega_r}. \tag{67}$$

It is clear that the commutation period of $i_{\rm pri}$ ($\Delta T_{1,4}$) only depends on ω_r, and it has no relationship with the operating frequency and the load condition. In order to shorten $\Delta T_{1,4}$, proper resonant parameters, shown in Fig. 10, should be selected. The relationship between $\Delta T_{1,2}$ and F with different Q_L's is clearly shown in Fig. 11 for practical design. Accordingly, the control criterion for D is also shown in Fig. 12. Here, the condition ($\Delta T_{1,2} < \Delta T_{1,4}$ in Fig. 11 or $D_{\min} < D_{\max}$ in Fig. 12) for ZCS operation of the two primary switches has a good accordance with the condition ($\lambda < 0$ in Fig. 9) for the soft commutation of $i_{\rm pri}$ on the bottom limitation of the operating frequency.

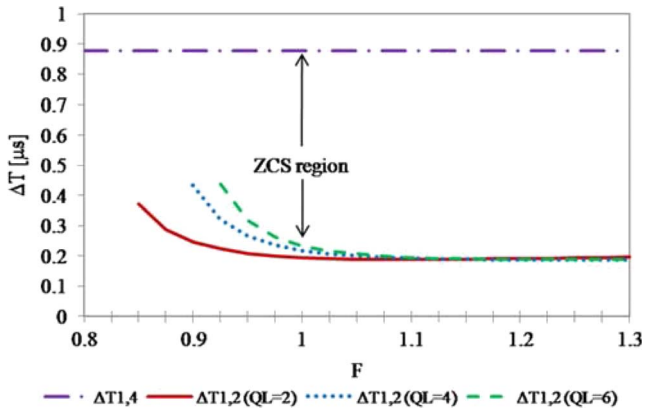

Fig. 11. Commutation times $\Delta T_{1,2}$ and $\Delta T_{1,4}$.

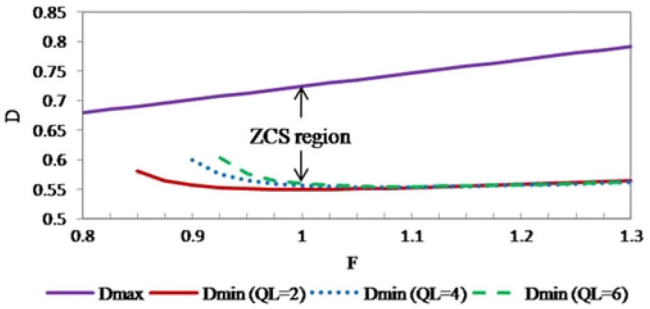

Fig. 12. Control criteria for duty cycle D.

E. ZCS Condition of Rectifying Diodes

As shown in Figs. 3 and 4, the essential for ZCS operation of the rectifying diodes is that i_{Lp} has to be charged up to i_{CS} before its commutation point, and α indicates this time margin. However, with the increase of the operating frequency, as shown in Fig. 9, i_{CS} would lead $v_{\rm rec}$ more and more, and hence, the margin α would decrease continuously until zero. If the operating frequency continually increases, the advanced commutation point of i_{CS} will finally cut down the conducting interval of the rectifying diodes; hence, there will not be enough time for i_{Lp} to be charged up to i_{CS} before its commutation point, and ZCS turn-off cannot be achieved for the rectifying diodes. Fig. 13 shows the simulation results that the rectifying diodes lose ZCS turn-off when the operating frequency (350 kHz) is much higher than the resonant frequency (250 kHz). The simulation circuit is based on the simplified circuit model shown in Fig. 3. Although the proposed converter also works without achieving ZCS for the rectifying diodes and the extended operating frequency is helpful to broaden the application of the proposed converter, the related discussion is beyond the scope of this paper.

The ZCS condition of the rectifying diodes is obtained as

$$\alpha \geq 0. \tag{68}$$

Fig. 14 describes the criterion (68) and indicates the top limitation of the operating frequency for achieving ZCS operation of the rectifying diodes.

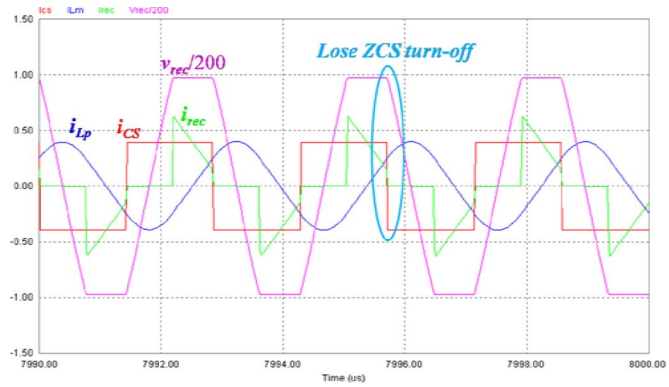

Fig. 13. Simulation results while the rectifying diodes are under hard switching.

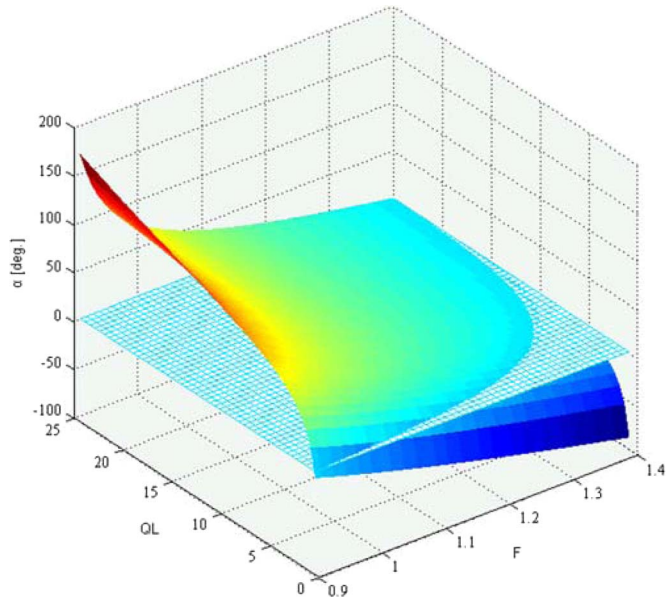

Fig. 14. ZCS margin α as a function of F and Q_L.

IV. Design Guideline

A. Resonant Tank Design

1) Set the resonant frequency ω_p.
2) From (46)–(48), set the operating frequency range and Q_L to fulfill the voltage regulation requirement, while maintain the ZCS condition for the primary switches.
3) Calculate the minimum voltage gain $G_{\rm min}$, and select the turns ratio of the transformer (N).
4) Calculate L_p and C_p from (2), (15), and (16) with the selected ω_p, R_L, and Q_L.
5) Calculate L_r from (50).
6) Manipulate all of these resonant components together with the circuit parasitics.

B. Duty Cycle Calculation

With the derived L_r, C_p, and N, the duty cycle limitation can be calculated from (55)–(57), (63), (64), (66), and (67). Practically, the duty cycle should be selected as close as possible to $D_{\rm max}$ to minimize the conduction of the antiparallel diode of

the MOSFET. This would be helpful not only in reducing the conduction loss but also in minimizing the reverse recovery of the antiparallel diode of the MOSFET.

C. Input Inductor Design

As shown in Fig. 2, the input current $i_{\rm in}$ rises up during the overlap time and declines during the off-time of any primary switches. Hence, $i_{\rm in}$ has the input ripple current of two times the switching frequency and the peak-to-peak amplitude of

$$\Delta i_{\rm in} = 2\frac{V_{\rm in}}{L}\Delta T_{ov} \tag{69}$$

where $L_{\rm in1}$ and $L_{\rm in2}$ are assumed to have the same value as L.

With the symmetrical operation of the current-fed half-bridge structure, the average current flowing through each input inductor $I_{\rm Lin}$ is equal to half of the input current $(I_{\rm in}/2)$.

As explained in part B, ΔT_{ov} can be substituted with $\Delta T_{1,4}$, and then, the design criterion for L can be obtained from (57), (63), (67), and (69) as

$$L = \frac{2\pi N V_{\rm in}\sqrt{L_r C_p}}{\Delta i_{\rm in}}. \tag{70}$$

D. Primary MOSFET Selection

With the single capacitor instead of LC for the output filter, the peak voltage of v_{AB} is clamped to $V_o/2N$. However, the existing resonance between L_r and the output capacitance of the primary MOSFET $(C_{\rm oss})$ induces an overshooting of v_{AB} when the MOSFET is turned off. An experiment-based empirical constant of 1.5 is accepted to represent such overshooting. Hence, the voltage stress on the primary MOSFETs is obtained as

$$V_{AB} = 1.5\frac{V_o}{N}. \tag{71}$$

With the modeled symmetrical square wave current source in Section III, the current flowing through each MOSFET could be considered as the pulse current with an amplitude of $I_{\rm in}$ and a duty cycle of 0.5. Hence, the rms current of each MOSFET is obtained as

$$I_{FET\_rms} = \frac{I_{\rm in}}{\sqrt{2}}. \tag{72}$$

E. Voltage Stress of the Rectifying Diodes

For the rectifying diodes, the off-time voltage is clamped to V_o, and ZCS turn-off is well ensured; hence, the voltage stress is V_o.

V. Experimental Results

The proposed converter in Fig. 1 was implemented as part of a PV module integrated converter (MIC), as shown in Fig. 15, with the following key specifications: maximum power point tracking (MPPT) range $V_{\rm in}$ is 23–38 V [49], output voltage V_o is 350 V, and maximum output power $P_{o\_\max}$ is 150 W.

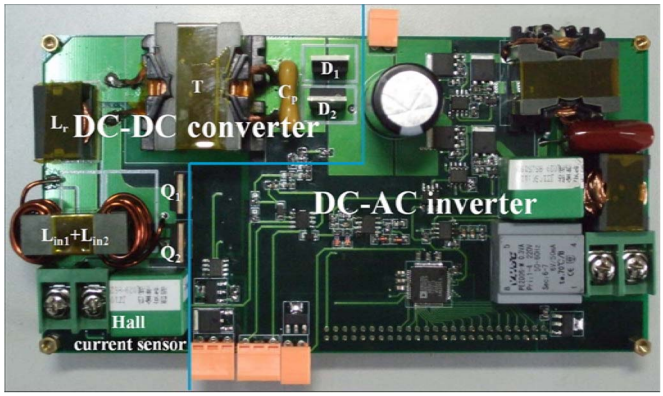

Fig. 15. Picture of the PV MIC prototype with the proposed converter adopted as the dc–dc part.

Besides the PV modules supported by Solarfun, major components of the prototype are listed as the following: $\rm Q_1$ and $\rm Q_2$ (IRFB4115GPbF), $\rm D_1$ and $\rm D_2$ (MUR860), transformer core (PC44PQ32/30Z-12) and turns ratio $(N_1 : N_2 = 5 : 14)$, $L_p = 89\ \mu$H, $L_r = 2.24\ \mu$H, $C_p = 4.29$ nF, $L_{in1} = L_{in2} = 100\ \mu$H, and $C_1 = C_2 = 2.2\ \mu$F. The input capacitor $C_{\rm in}$ was not applied for the experimental illustration of the small input current ripple property of the proposed converter. Pulse frequency modulation is adopted as the control method, and FPGA acts as the controller. ADP3624ARDZ with 3.3-V compatible inputs and dual channel common ground 4-A high-speed driving is selected as the driver.

Figs. 16–22 show the experimental waveforms of the prototype with an optimum design for $V_{\rm in} = 23$ V, $V_o = 350$ V, and switching frequency $f_s = 255$ kHz. Fig. 16(a)–(c) shows v_{AB} and $i_{\rm pri}$ at full, 20%, and 5% loads. v_{g1} and v_{g2} are the driving signals of $\rm Q_1$ and $\rm Q_2$, respectively. The waveforms show that, in full load range, two primary switches are both turned off with ZCS, the voltage spikes and current overshooting are very small, and no additional clamping circuit is necessary. The oscillation of v_{AB} is mainly caused by the reverse recovery of $\rm D_{Q1}$ and $\rm D_{Q2}$. Although the reverse recovery of the low-voltage MOSFETs' antiparallel diodes is not severe, it is suggested to seriously evaluate the reverse recovery performance of the antiparallel diode when selecting the MOSFET. An external antiparallel Schottky diode would be preferred to bypass the internal intrinsic diode if necessary.

It is clear that, as the load comes to light, the decreased load current conduction period releases the clamping of v_{Cp}, and such mechanism enables downward resonance of v_{Cp} and generates lower initial energy for the resonance among L_r, L_p, and C_p. Although the leakage inductance is still designed according to heavy load condition for the purpose of ensuring full load range ZCS operation of the primary switches, the overshooting of $i_{\rm pri}$ is reduced, and a little redundant circulating current flows through the antiparallel diodes. Thereby, the necessary circulating energy for the ZCS operation of the primary switches is adaptive to the load and can be very low, and the light load efficiency is not affected.

In Fig. 16(a)–(c), another important feature of the proposed converter is revealed, i.e., the turn-on voltage of the primary MOSFET also comes down as the load decreases. Hence, it

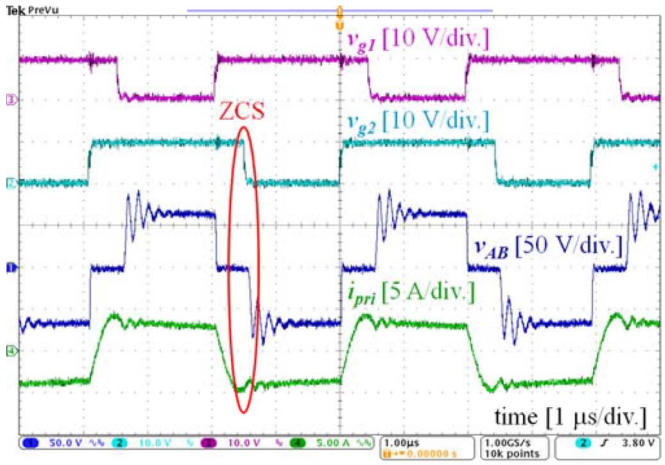

(a)

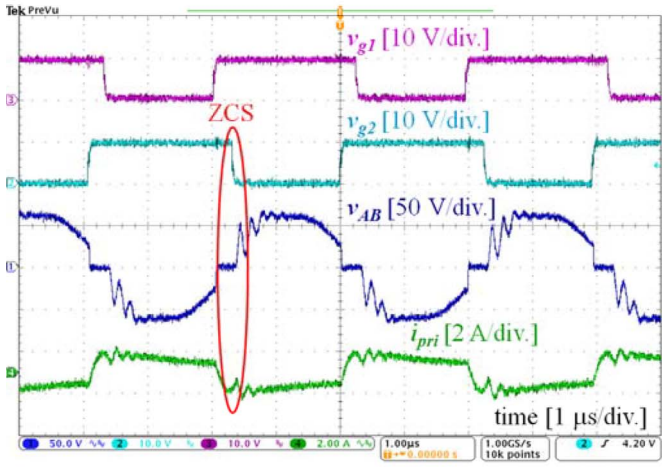

(b)

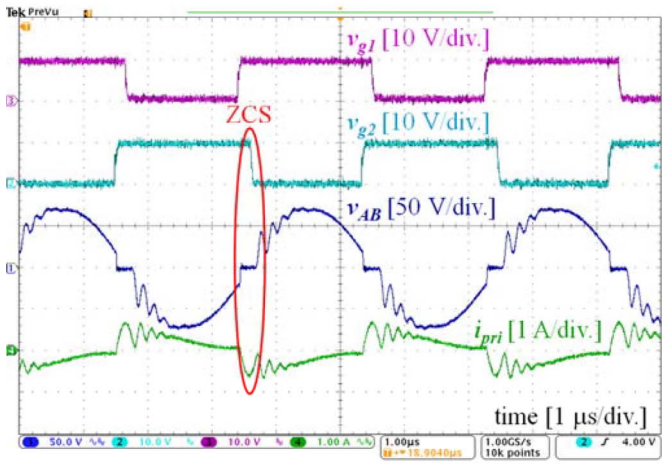

(c)

Fig. 16. Waveforms of v_{g1}, v_{g2}, v_{AB}, and $i_{\rm pri}$ at (a) full, (b) 20%, and (c) 5% loads.

can be concluded that quasi-ZVS is achieved at light load, and this is also helpful in improving the light load efficiency of the proposed converter.

The primary active switches have the failure risk when their ZCS cannot be achieved. However, by following the proposed design method in Section III-D, a stable ZCS margin can be ensured, and little failure risk comes to the practical. Fig. 17 shows the waveforms of v_{AB} and $i_{\rm pri}$ when the proposed

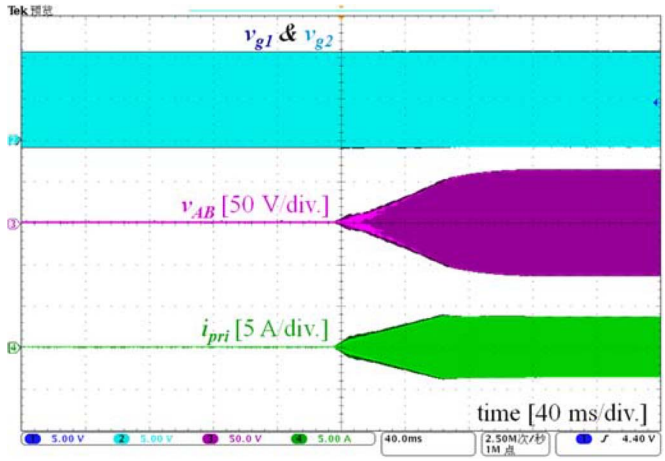

Fig. 17. Full load direct startup waveforms of v_{AB} and $i_{\rm pri}$.

converter starts up without any soft start techniques at full load. Hence, the robust ZCS operation of the primary active switches in the proposed converter is well demonstrated by Figs. 16 and 17.

However, if the freewheeling path of the two input inductors' current is broken in case of the gate driver or auxiliary power supply losing earlier than the input power, it will destroy the primary active switches. This is a common issue for current-fed converters no matter if push–pull half- or full-bridge structures are adopted as a current source generator. Such kind of situation should be greatly taken care of and can be well handled in practical engineering.

Fig. 18(a) and (b) shows the v_{Cp}, the voltage of $\rm D_2$ (v_{D2}), and the current flowing through the rectifying diodes $(i_{\rm rec})$ at full and 20% loads, respectively. It can be seen that v_{Cp} is clamped to $V_o/2$ for most of the switching cycle at full load. Therefore, the circulating energy within the resonant tank is small. v_{D2} is clamped to V_o without any overshooting. $i_{\rm rec}$ decreases to zero with low slew rate. Thereby, ZCS operation is also well achieved for all of the rectifying diodes.

Fig. 19 shows $i_{\rm in}$, i_{Lin1}, and V_o when the two input inductors are not coupled together. i_{Lin2} is similar to i_{Lin1} but with 180° phase shift; hence, the current ripple of $i_{\rm in}$ is very small, and its frequency is twice the switching frequency. Then, a small cost-effective nonpolarity cap would be enough to filter the input ripple current. Although two input inductors seem bulky compared to the voltage-fed converters, the proposed CFMRC eliminates the bulky input current ripple filters in which the electrolytic capacitors are always necessary but have much shorter lifetime compared to the inductors. Hence, the two input inductors will not impact the volume of the whole converter, but they promise a longer lifetime to the converter. Since the input current is relatively high, the two input inductors share the input current, which not only reduces the primary current of the transformer and the related conduction losses but also releases the design and thermal stress of the inductor itself compared to a single inductor.

For further power density and efficiency improvement, coupled inductor techniques are finally applied to the two input inductors. Fig. 20 shows the related waveforms. Compared to the noncoupled inductors, coupled inductor techniques help in

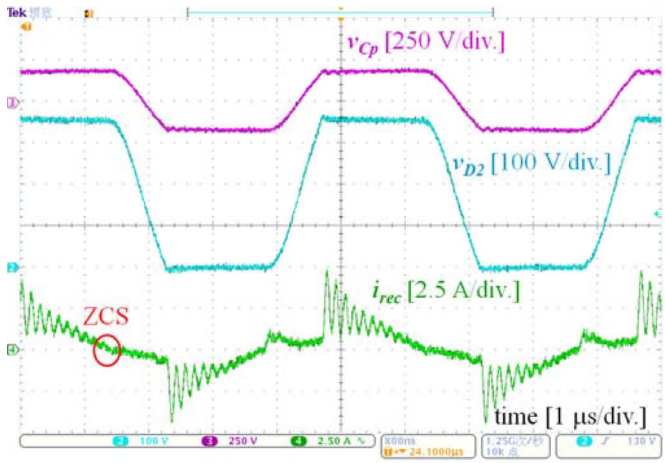

(a)

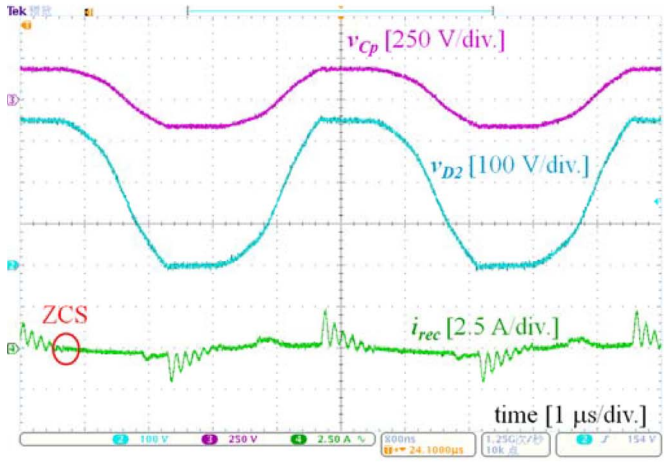

(b)

Fig. 18. Waveforms of v_{Cp}, v_{D2}, and $i_{\rm rec}$ at (a) full and (b) 20% loads.

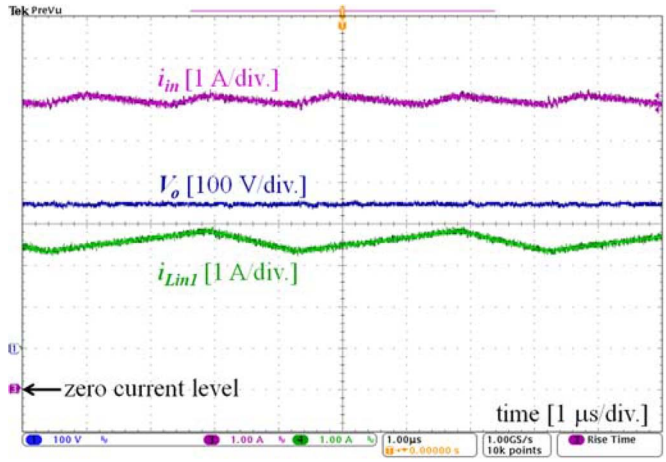

Fig. 19. Full load waveforms of $i_{\rm in}$, i_{Lin1}, and V_o without coupling the input inductors.

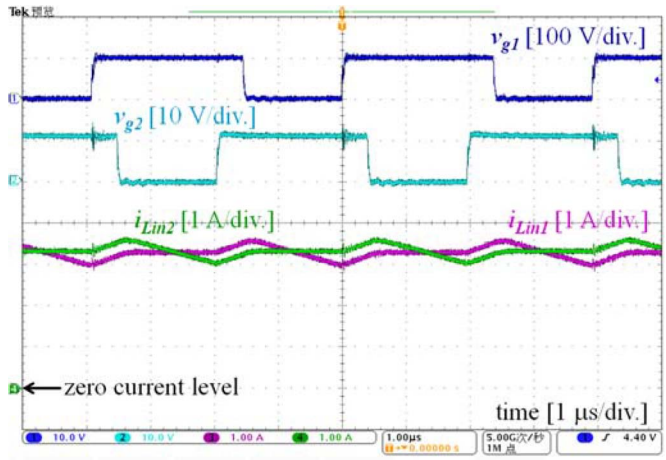

Fig. 20. Full load waveforms of i_{Lin1} and i_{Lin2} with the applied coupled inductors.

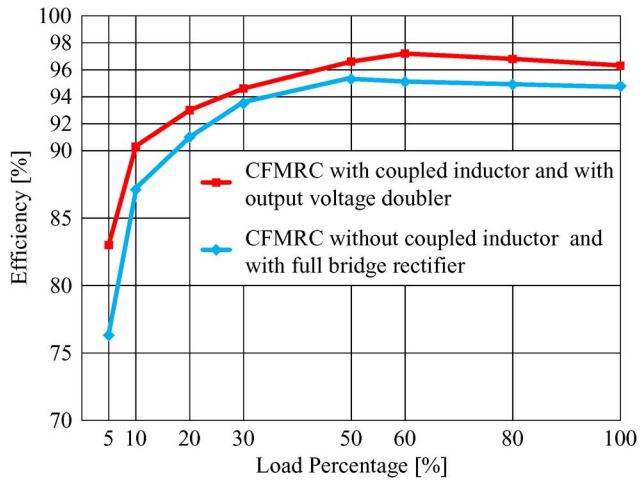

Fig. 21. Measured efficiency curve.

reducing the inductance from 100 to 80 μH and, with only one core (3C96-E28/17/11+I28/3.5/11) for the same current ripple, cancel part of the magnetic fluxes, hence reducing both core and copper losses.

Fig. 21 shows the measured efficiency curve with four FLUKE 289 multimeters within full load range. A peak efficiency of 97.2% is achieved at 60% load, and the full load efficiency is 96.2%.

Fig. 22 shows the loss breakdown results at full load for the proposed converter, and the unit is Wart. In Fig. 22, $P_{\rm other}$ represents a summary of the losses caused by the reverse recovery of $\rm D_{Q1}$ and $\rm D_{Q2}$, the losses induced by the parasitic ringing, and the losses on the PCB circuits and terminations.

Obviously, copper losses occupy the most 30% of the total loss. The copper losses are mainly induced by the magnetizing current. Compared with large resonant current flowing through the parallel resonant inductor L_p in conventional CFPRCs with LC output filter [32], such magnetizing current is limited and is essential in keeping the high boost capability and in achieving ZCS of the rectifying diodes of the proposed converter. Moreover, the unavoidable magnetizing current only circulates in the resonant tank, without going through the switching networks; hence, the current rating of the silicon devices is not affected, and only the secondary winding of the transformer should be designed with proper copper to reduce the conduction loss.

In Fig. 22, the turn-on losses of the two primary MOSFETs take up almost 9% total loss. However, as the load decreases, the turn-on voltage will decrease quickly and will not affect

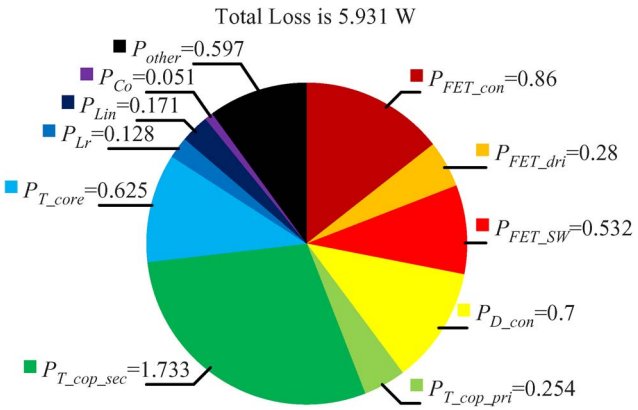

Fig. 22. Loss breakdown of the proposed converter.

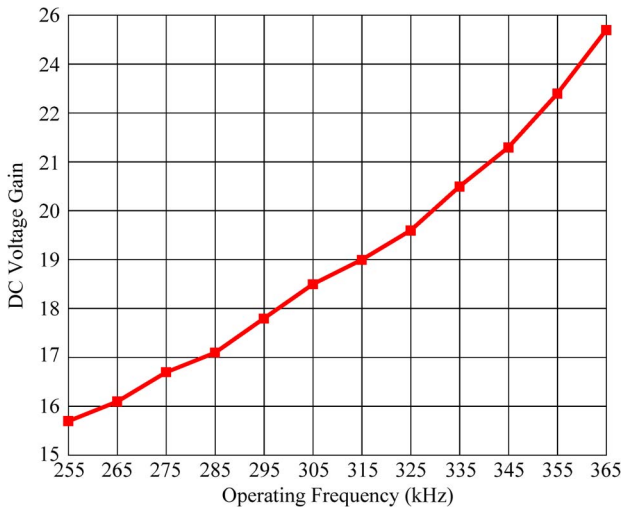

Fig. 23. Measured gain curve with the specified parameters.

the light load efficiency much as aforementioned. Moreover, even for lower input voltage applications, the hard switching-on impact for the efficiency will be much smaller. Moreover, the proposed converter certainly has the potential of achieving much higher dc gain while maintaining high efficiency as more than 15 times dc gain has already been achieved with a turns ratio of only 5:14 in the current prototype.

Fig. 23 shows the measured dc voltage gain of the proposed converter. With the designed parameters ($Q_L = 5.6$ and $N = 2.8$), the experimental results demonstrate well the calculated and simulated results shown in Fig. 8.

Finally, some modifications are applied to the resonant tank to meet the wide input voltage requirement. The efficiency data with different input voltages at full load have been collected and shown in Fig. 24. Here, the efficiency is 95.3%, with a 23-V input at full load. There is about 0.9% efficiency drop compared to an optimum dc transformer oriented design. However, the efficiency curve is flat over the entire MPPT range, an average efficiency of 95.9% was achieved, and a maximum efficiency of 96.5% was recorded at a 38-V input.

VI. Conclusion

A novel high-efficiency high step-up dc–dc converter with low input ripple current has been proposed for interfacing the

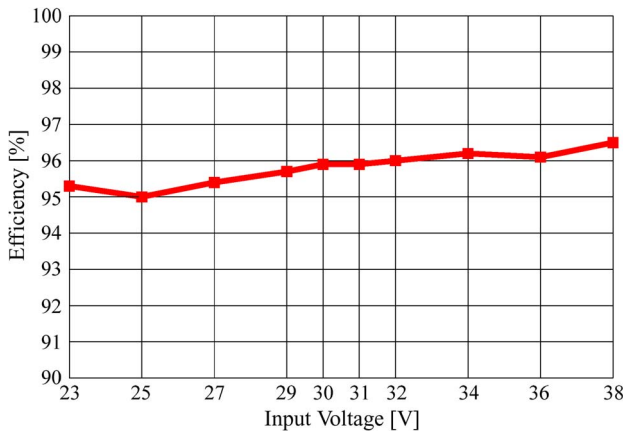

Fig. 24. Efficiency data with different input voltages at full load.

sustainable power sources, such as PV panels and fuel cells, which are characterized by low-voltage high-current output and have strict current ripple requirement.

The operation principle of the proposed converter is well introduced. The current-fed half-bridge structure promises low input current ripple, low primary current of the transformer, high step-up capability, and common ground gate driving. The multiresonant tank creates ZCS condition for the primary switches, provides high voltage gain, and fully utilizes the parasitic parameters of the transformer. The adopted single-capacitor output filter helps in reducing the circulating energy, in limiting the overshooting of the primary current, and in achieving ZCS for the rectifying diodes all in full load range. In order to further improve the performances of the proposed converter, coupled inductor and voltage doubler techniques were finally applied. All of these features guarantee the high performance of the proposed converter.

Based on a comprehensive steady-state analysis for the proposed converter, the dc voltage gain and the ZCS conditions of all active switches are derived. A design guideline for the proposed converter is also developed.

Withal, it is found that the proposed converter also works when the switching frequency exceeds its top limitation for ZCS operation of the rectifying diodes. However, the related discussion is beyond the scope of this paper.

The theoretical analysis and the merits of the proposed converter are verified on a 150-W prototype. An average efficiency of 95.9% was achieved over the entire MPPT range (23–38 V), with a 350-V output at full load.

References

[1] F. Blaabjerg, Z. Chen, and S. B. Kjaer, "Power electronics as efficient interface in dispersed power generation systems," *IEEE Trans. Power Electron.*, vol. 19, no. 5, pp. 1184–1194, Sep. 2004.

[2] M. Carrasco, L. G. Franquelo, J. T. Bialasiewicz, E. Galvan, R. C. Portillo Guisado, M. A. M. Prats, J. I. Leon, and N. Moreno-Alfonso, "Power-electronic systems for the grid integration of renewable energy sources: A survey," *IEEE Trans. Ind. Electron.*, vol. 53, no. 4, pp. 1002–1016, Jun. 2006.

[3] G. Fontes, C. Turpin, S. Astier, and T. A. Meynard, "Interactions between fuel cell and power converters: Influence of current harmonics on a fuel cell stack," *IEEE Trans. Power Electron.*, vol. 22, no. 2, pp. 670–678, Mar. 2007.

[4] R. J. Wai, C. Y. Lin, and Y. R. Chang, "High step-up bidirectional isolated converter with two input power sources," *IEEE Trans. Ind. Electron.*, vol. 56, no. 7, pp. 2629–2643, Jul. 2009.

[5] M. Cacciato, A. Consoli, R. Attanasio, and F. Gennaro, "Soft-switching converter with HF transformer for grid-connected photovoltaic systems," *IEEE Trans. Ind. Electron.*, vol. 57, no. 5, pp. 1678–1686, May 2010.

[6] S. V. Araujo, R. P. Torrico-Bascope, and G. V. Torrico-Bascope, "Highly efficient high step-up converter for fuel-cell power processing based on three-state commutation cell," *IEEE Trans. Ind. Electron.*, vol. 57, no. 6, pp. 1987–1997, Jun. 2010.

[7] C. T. Pan and C. M. Lai, "A high-efficiency high step-up converter with low switch voltage stress for fuel-cell system applications," *IEEE Trans. Ind. Electron.*, vol. 57, no. 6, pp. 1998–2006, Jun. 2010.

[8] S. K. Changchien, T. J. Liang, J. F. Chen, and L. S. Yang, "Novel high step-up dc–dc converter for fuel cell energy conversion system," *IEEE Trans. Ind. Electron.*, vol. 57, no. 6, pp. 2007–2017, Jun. 2010.

[9] M. Mohr, W. T. Franke, B. Wittig, and F. W. Fuchs, "Converter systems for fuel cells in the medium power range—A comparative study," *IEEE Trans. Ind. Electron.*, vol. 57, no. 6, pp. 2024–2032, Jun. 2010.

[10] A. Giustiniani, G. Petrone, G. Spagnuolo, and M. Vitelli, "Low-frequency current oscillations and maximum power point tracking in grid-connected fuel-cell-based systems," *IEEE Trans. Ind. Electron.*, vol. 57, no. 6, pp. 2042–2053, Jun. 2010.

[11] R. J. Wai and C. Y. Lin, "Active low-frequency ripple control for clean-energy power-conditioning mechanism," *IEEE Trans. Ind. Electron.*, vol. 57, no. 11, pp. 3780–3792, Nov. 2010.

[12] A. Shahin, M. Hinaje, J. P. Martin, S. Pierfederici, S. Rael, and B. Davat, "High voltage ratio dc–dc converter for fuel-cell applications," *IEEE Trans. Ind. Electron.*, vol. 57, no. 12, pp. 3944–3955, Dec. 2010.

[13] D. Vinnikov and I. Roasto, "Quasi-Z-source-based isolated dc/dc converters for distributed power generation," *IEEE Trans. Ind. Electron.*, vol. 58, no. 1, pp. 192–201, Jan. 2011.

[14] A. I. Bratcu, I. Munteanu, S. Bacha, D. Picault, and B. Raison, "Cascaded dc–dc converter photovoltaic systems: Power optimization issues," *IEEE Trans. Ind. Electron.*, vol. 58, no. 2, pp. 403–411, Feb. 2011.

[15] J. K. Park, W. Y. Choi, and B. H. Kwon, "A step-up dc–dc converter with a resonant voltage doubler," *IEEE Trans. Ind. Electron.*, vol. 54, no. 6, pp. 3267–3275, Dec. 2007.

[16] C. S. Leu and M. H. Li, "A novel current-fed boost converter with ripple reduction for high-voltage conversion applications," *IEEE Trans. Ind. Electron.*, vol. 57, no. 6, pp. 2018–2023, Jun. 2010.

[17] P. J. Wolfs, "A current-sourced dc–dc converter derived via the duality principle from the half-bridge converter," *IEEE Trans. Ind. Electron.*, vol. 40, no. 1, pp. 139–144, Feb. 1993.

[18] M. H. Todorovic, L. Palma, and P. N. Enjeti, "Design of a wide input range dc–dc converter with a robust power control scheme suitable for fuel cell power conversion," *IEEE Trans. Ind. Electron.*, vol. 55, no. 3, pp. 1247–1255, Mar. 2008.

[19] S. S. Lee, S. W. Rhee, and G. W. Moon, "Coupled inductor incorporated boost half-bridge converter with wide ZVS operation range," *IEEE Trans. Ind. Electron.*, vol. 56, no. 7, pp. 2505–2512, Jul. 2009.

[20] J. F. Chen, R. Y. Chen, and T. J. Liang, "Study and implementation of a single-stage current-fed boost PFC converter with ZCS for high voltage applications," *IEEE Trans. Power Electron.*, vol. 23, no. 1, pp. 379–386, Jan. 2008.

[21] R. Y. Chen, T. J. Liang, J. F. Chen, R. L. Lin, and K. C. Tseng, "Study and implementation of a current-fed full-bridge boost dc–dc converter with zero-current switching for high-voltage applications," *IEEE Trans. Ind. Appl.*, vol. 44, no. 4, pp. 1218–1226, Jul./Aug. 2008.

[22] H. Wang, Q. Sun, H. S. H. Chung, S. Tapuchi, and A. Ioinovici, "A ZCS current-fed full-bridge PWM converter with self-adaptable soft-switching snubber energy," *IEEE Trans. Power Electron.*, vol. 24, no. 8, pp. 1977–1991, Aug. 2009.

[23] M. Nymand and M. A. E. Andersen, "High-efficiency isolated boost dc–dc converter for high-power low-voltage fuel-cell applications," *IEEE Trans. Ind. Electron.*, vol. 57, no. 2, pp. 505–514, Feb. 2010.

[24] S. K. Han, H. K. Yoon, G. W. Moon, M. J. Youn, Y. H. Kim, and K. H. Lee, "A new active clamping zero-voltage switching PWM current fed half-bridge converter," *IEEE Trans. Power Electron.*, vol. 20, no. 6, pp. 1271–1279, Nov. 2005.

[25] S. J. Jang, C. Y. Won, B. K. Lee, and J. Hur, "Fuel cell generation system with a new active clamping current-fed half-bridge converter," *IEEE Trans. Energy Convers.*, vol. 22, no. 2, pp. 332–340, Jun. 2007.

[26] J. M. Kwon and B. H. Kwon, "High step-up active-clamp converter with input-current doubler and output-voltage doubler for fuel cell power systems," *IEEE Trans. Power Electron.*, vol. 24, no. 1, pp. 108–115, Jan. 2009.

[27] J. M. Kwon, E. H. Kim, B. H. Kwon, and K. H. Nam, "High-efficient fuel cell power conditioning system with input current ripple reduction," *IEEE Trans. Ind. Electron.*, vol. 56, no. 3, pp. 826–834, Mar. 2009.

[28] S. Jalbrzykowski and T. Citko, "Current-fed resonant full-bridge boost dc/ac/dc converter," *IEEE Trans. Ind. Electron.*, vol. 55, no. 3, pp. 1198–1205, Mar. 2008.

[29] D. Fu, B. Lu, and F. C. Lee, "1 MHz high efficiency LLC resonant converters with synchronous rectifier," in *Proc. IEEE Power Electron. Spec. Conf.*, 2007, pp. 2404–2410.

[30] D. Fu, F. C. Lee, Y. Liu, and M. Xu, "Novel multi-element resonant converters for front-end dc/dc converters," in *Proc. IEEE Power Electron. Spec. Conf.*, 2008, pp. 250–256.

[31] D. Fu, F. C. Lee, Y. Qiu, and F. Wang, "A novel high-power-density three-level LCC resonant converter with constant-power-factor-control for charging applications," *IEEE Trans. Power Electron.*, vol. 23, no. 5, pp. 2411–2420, Sep. 2008.

[32] D. Fu, "Topology investigation and system optimization of resonant converters," Ph.D. dissertation, Virginia Polytechnic Inst. State Univ., Blacksburg, VA, 2010.

[33] T. Ninomiya, T. Higashi, and K. Harada, "Analysis of the static and dynamic characteristics of push–pull parallel resonant converters," in *Proc. IEEE Power Electron. Spec. Conf.*, 1986, pp. 367–374.

[34] G. Ivensky, A. Abramovitz, M. Gulko, and S. B. Yaakov, "A resonant dc–dc transformer," *IEEE Trans. Aerosp. Electron. Syst.*, vol. 29, no. 3, pp. 926–934, Jul. 1993.

[35] D. Edry and S. B. Yaakov, "Capacitive-loaded push–pull parallel-resonant converter," *IEEE Trans. Aerosp. Electron. Syst.*, vol. 29, no. 4, pp. 1287–1296, Oct. 1993.

[36] G. Ivensky, M. Gulko, and S. B. Yaakov, "Current-fed multiresonant isolated dc–dc converter," *IEEE Trans. Aerosp. Electron. Syst.*, vol. 33, no. 1, pp. 53–63, Jan. 1997.

[37] M. K. Kazimierczuk and A. Abdulkarim, "Current-source parallel resonant dc/dc converter," *IEEE Trans. Ind. Electron.*, vol. 42, no. 2, pp. 199–208, Apr. 1995.

[38] J. M. Alonso, J. García, A. J. Calleja, J. Ribas, and J. Cardesín, "Analysis, design, and experimentation of a high-voltage power supply for ozone generation based on current-fed parallel-resonant push–pull inverter," *IEEE Trans. Ind. Appl.*, vol. 41, no. 5, pp. 1364–1372, Sep./Oct. 2005.

[39] D. J. Thrimawithana and U. K. Madawala, "Analysis of split-capacitor push–pull parallel-resonant converter in boost mode," *IEEE Trans. Power Electron.*, vol. 23, no. 1, pp. 359–368, Jan. 2008.

[40] Y. Ren, M. Xu, J. Zhou, and F. C. Lee, "Analytical loss model of power MOSFET," *IEEE Trans. Power Electron.*, vol. 21, no. 2, pp. 310–319, Mar. 2006.

[41] M. Matsuo, T. Suetsugu, S. Mori, and I. Sasase, "Class DE current-source parallel resonant inverter," *IEEE Trans. Ind. Electron.*, vol. 46, no. 2, pp. 242–248, Apr. 1999.

[42] T. J. Liang, R. Y. Chen, and J. F. Chen, "Current-fed parallel-resonant dc–ac inverter for cold-cathode fluorescent lamps with zero-current switching," *IEEE Trans. Power Electron.*, vol. 23, no. 4, pp. 2206–2210, Jul. 2008.

[43] F. J. Lin, R. Y. Duan, and J. C. Yu, "An ultrasonic motor drive using a current-source parallel-resonant inverter with energy feedback," *IEEE Trans. Power Electron.*, vol. 14, no. 1, pp. 31–42, Jan. 1999.

[44] M. Xu, Y. Ying, Q. Li, and F. C. Lee, "Novel coupled-inductor multi-phase VRs," in *Proc. IEEE APEC*, 2007, pp. 113–119.

[45] G. Ivensky, A. Kats, and S. B. Yaakov, "An RC load model of parallel and series-parallel resonant dc–dc converters with capacitive output filter," *IEEE Trans. Power Electron.*, vol. 14, no. 3, pp. 515–521, May 1999.

[46] A. J. Forsyth, G. A. Ward, and S. V. Mollov, "Extended fundamental frequency analysis of the LCC resonant converter," *IEEE Trans. Power Electron.*, vol. 18, no. 6, pp. 1286–1292, Nov. 2003.

[47] J. A. Martin-Ramos, J. Diaz, A. M. Pernia, J. M. Lopera, and F. Nuno, "Dynamic and steady-state models for the PRC-LCC resonant topology with a capacitor as output filter," *IEEE Trans. Ind. Electron.*, vol. 54, no. 4, pp. 2262–2275, Aug. 2007.

[48] J. A. M. Ramos, A. M. Pernia, J. Diaz, F. Nuno, and J. A. Martinez, "Power supply for a high-voltage application," *IEEE Trans. Power Electron.*, vol. 23, no. 4, pp. 1608–1619, Jul. 2008.

[49] S. B. Kjaer, "Design and control of an inverter for photovoltaic applications," Ph.D. dissertation, Inst. Energy Technol., Aalborg Univ., Aalborg East, Denmark, 2005.

Bo Yuan (S'07) was born in China in 1981. He received the B.S., M.S., and Ph.D. degrees in electrical engineering from Xi'an Jiaotong University, Xi'an, China, in 2005, 2007, and 2011, respectively.

He was an Intern with FSP-Powerland Technology, Inc., Xi'an; Delta Hangzhou Design Center, Hangzhou; and the Power Management Products (PMP) Division, Analog Devices, Inc., Shanghai, in the summer of 2008, 2009, and 2010, respectively. He is now with the PMP Division, Analog Devices, Inc., Xi'an, Shaanxi 710075 China, where he engages in developing digital power supply systems.

Xu Yang (M'02) was born in China in 1972. He received the B.S. and Ph.D. degrees in electrical engineering from Xi'an Jiaotong University, Xi'an, China, in 1994 and 1999, respectively.

He has been a member of the faculty of the School of Electrical Engineering, Xi'an Jiaotong University, since 1999, where he is presently a Professor. From November 2004 to November 2005, he was a Visiting Scholar with the Center of Power Electronics Systems, Virginia Polytechnic Institute and State University, Blacksburg. He then came back to Xi'an Jiaotong University and engaged in teaching and research in the power electronics and industrial automation areas. His research interests include soft-switching topologies, pulsewidth modulation control techniques and power electronic integration, and packaging technologies.

Xiangjun Zeng was born in China in 1975. He received the B.S., M.S., and Ph.D. degrees in electrical engineering from Xi'an Jiaotong University, Xi'an, China, in 1998, 2001, and 2005, respectively.

From 2006 to 2007, he was with Aalborg University, Aalborg, Denmark, as a Visiting Scholar. He then came back to Xi'an Jiaotong University and engaged in teaching and research in the power electronics area. His research interests include renewable energy harvesting and power electronic integration technologies.

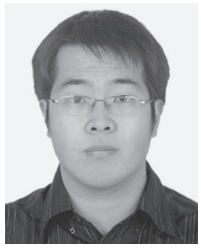

Jason Duan (M'10) was born in China in 1978. He received the B.S. and M.S. degrees in electrical engineering from Xi'an Jiaotong University, Xi'an, China, in 2000 and 2003, respectively.

He was with Delta Power Electronic Center, Shanghai, China, in 2003. He joined the Power Management Products Division, Analog Devices, Inc., Shanghai, in 2007, where he engages in developing digital power supply systems.

Jerry Zhai was born in China in 1967. He received the B.S. degree in electrical engineering from the Huazhong University of Science and Technology, Wuhan, China, in 1988 and the Ph.D. degree in electrical engineering from Zhejiang University, Hangzhou, China, in 1994.

He is currently the Director of the Power Management Products Division, Analog Devices, Inc., Shanghai, China, and is responsible for the power IC development and regional marketing and business development. He is also responsible in leading the power management application team for the Asian country sales.

Donghao Li was born in China in 1986. He received the B.S. degree in electrical engineering from the Taiyuan University of Science and Technology, Taiyuan, China, in 2008 and the M.S. degree in electrical engineering from Xi'an Jiaotong University, Xi'an, China, in 2011.

He is currently with the Second Academy of China Aerospace, Beijing, China, where he engages in developing power supplies with high reliability for aerospace application. His research interest is soft-switching topologies.